Journal of Materials Chemistry C

ROYAL SOCIETY OF CHEMISTRY

PAPER

View Article Online
View Journal | View Issue

Check for updates

Cite this: J. Mater. Chem. C, 2025, 13, 10062

Research on the $Ga_2O_3/ZnGa_2O_4$ mixed-phase films and solar-blind photodetectors prepared directly by annealing Zn alloying Ga_2O_3 films†

Mingshuo Wang,[ab] Xing Chen,*[ab] Kewei Liu,*[ab] Xuan Sun,[ab] Xiaoqian Huang,[ab] Jialin Yang,[a] Yongxue Zhu,[a] Zhen Cheng,[a] Binghui Li[a] and Dezhen Shen*[abc]

High-Zn-content doped β-Ga_2O_3 thin films were grown on *c*-plane sapphire substrates using metal–organic chemical vapor deposition (MOCVD), with subsequent annealing inducing a phase transition, converting the initially single-phase material into a $Ga_2O_3/ZnGa_2O_4$ mixed-phase structure. Furthermore, metal–semiconductor–metal structured solar-blind photodetectors were fabricated to evaluate the ultraviolet detection capabilities of these mixed-phase films. The detector performance was significantly enhanced following annealing. At an annealing temperature of 800 °C, phase separation occurred, and the improvement in device performance became more pronounced. Devices annealed in an argon atmosphere, undergoing phase separation, exhibited superior optoelectronic performance, achieving a low dark current of 0.137 pA at a bias voltage of 10 V. At the peak wavelength, the device also demonstrated a responsivity of 2058.54 A W^{-1}, a specific detectivity of 3.21 × 10^{15} cm $Hz^{1/2}$ W^{-1}, and a short decay time of 2.90 ms. The exceptional performance of mixed-phase devices is likely attributed to the large number of heterojunction interfaces between Ga_2O_3 and $ZnGa_2O_4$. This study investigates the transition of the thin film material from a single-phase to a mixed-phase structure, analyzing the associated changes in their physical properties and detector performance. Additionally, it expands the material design framework for Ga_2O_3-based ultraviolet photodetectors and introduces a novel strategy to enhance their performance.

Received 18th February 2025,
Accepted 9th April 2025

DOI: 10.1039/d5tc00710k

rsc.li/materials-c

Open Access Article. Published on 22 April 2025. Downloaded on 1/10/2026 3:24:16 PM.
This article is licensed under a Creative Commons Attribution-NonCommercial 3.0 Unported Licence.

Introduction

Ultraviolet detection technology holds significant market potential and covers diverse consumer electronics and industry applications, such as automotive, pharmaceutical, medical diagnostics, environmental monitoring and industrial process control, among others.[1] Ultraviolet light in the range of 200–280 nm in the solar spectrum is strongly absorbed by ozone in the atmosphere and cannot reach the surface of the Earth, so this band of ultraviolet is called the solar-blind ultraviolet band. As a result, detectors operating in these specific wavelengths exhibit lower noise levels and higher sensitivity.[2–4] Wide-bandgap semiconductor materials offer distinct advantages, including an intrinsic bandgap ideally suited for ultraviolet detection and excellent stability. These characteristics have made them the focus of growing interest and research in this field.[5–7] Typically, detectors fabricated from single-phase materials are more commonly used, as they generally offer superior performance compared to their mixed-phase counterparts.[8–10] However, a study conducted by our group in 2014 demonstrated that ultraviolet detectors made from mixed-phase MgZnO thin films could achieve performance comparable to that of single-phase devices.[11] Building on this, Han *et al.* conducted additional research, validating the ultraviolet response characteristics of mixed-phase MgZnO thin films.[12,13] In recent years, Ga_2O_3 has garnered significant attention due to its exceptional physical properties,[14] leading to a growing body of research on solar-blind ultraviolet detectors.[15–21] Concurrently, studies on Ga_2O_3-based mixed-phase structural films have emerged as a prominent area of investigation. Researchers have successfully obtained mixed-phase Ga_2O_3 films by optimizing the growth conditions.[22,23] Liu *et al.* improved the sensitivity and signal-to-noise ratio of

[a] State Key Laboratory of Luminescence Science and Technology, Changchun Institute of Optics, Fine Mechanics and Physics, Chinese Academy of Sciences, Changchun 130033, People's Republic of China. E-mail: chenxing@ciomp.ac.cn, liukw@ciomp.ac.cn, shendz@ciomp.ac.cn
[b] Center of Materials Science and Optoelectronics Engineering, University of Chinese Academy of Sciences, Beijing, 100049, People's Republic of China
[c] Gusu Lab, Suzhou, 215125, People's Republic of China

† Electronic supplementary information (ESI) available: AFM, EDS, and performance of films annealing under different conditions. See DOI: https://doi.org/10.1039/d5tc00710k

This journal is © The Royal Society of Chemistry 2025

Open Access Article. Published on 22 April 2025. Downloaded on 1/10/2026 3:24:16 PM. This article is licensed under a Creative Commons Attribution-NonCommercial 3.0 Unported Licence.

devices by utilizing amorphous/β-Ga_2O_3 films.[24] Alghareeb *et al.* grew mixed γ/β-Ga_2O_3 films on n-type Si, resulting in detectors with enhanced overall performance.[25] Furthermore, the incorporation of excess doping elements during the Ga_2O_3 growth process, beyond their solubility limits, can induce the formation of mixed-phase structures.[26,27] Fan *et al.* prepared a mixed-phase thin film by heating a mixture of Ga_2O_3 and SnO_2 powders in a tube furnace.[28] Qi *et al.* controlled the precursor ratio of In and Ga to grow $(In_xGa_{1-x})_2O_3$ thin films, which exhibited coexistence of monoclinic and cubic phases.[29] Current research predominantly focuses on the direct synthesis of mixed-phase materials. In contrast, studies investigating the phase transition from single-phase to mixed-phase materials, as well as comparative analyses of the properties and device performance of single-phase *versus* mixed-phase materials, remain relatively scarce.

In this work, we employed metal organic chemical vapor deposition (MOCVD) to grow a single-phase Zn-alloyed Ga_2O_3 thin film with an approximate Zn composition of 15 at% on a sapphire (*c*-plane) substrate. Subsequently, the film was annealed to induce a phase transition, resulting in the formation of a mixed-phase structure. The Ga_2O_3 thin films were annealed in oxygen and argon atmospheres to investigate their structural and physical properties. Based on these films, a metal–semiconductor–metal (MSM) detector was fabricated to evaluate the impact of the $Ga_2O_3/ZnGa_2O_4$ mixed-phase structure on ultraviolet detection performance. The detector annealed at 800 °C in an argon atmosphere demonstrated superior detection performance. Under a 10 V bias, the dark current was below 1 pA, with a decay time of 2.90 ms. The responsivity at the peak wavelength was 2058.54 A W^{-1}. The substantial enhancement in device performance may be attributed to the formation of heterojunction interfaces between the mixed-phases within the thin films. Our findings in this work show promising prospects for $Ga_2O_3/ZnGa_2O_4$ mixed-phase photodetectors in solar-blind photodetection applications.

Experimental

Ga_2O_3 thin films alloyed with approximately 15 at% Zn were epitaxially grown on c-Al_2O_3 substrates *via* MOCVD. High-purity nitrogen was used as the carrier gas for diethylzinc (DEZn) and triethylgallium (TEGa), with 99.999% oxygen as the reactant gas. The source temperatures of DEZn and TEGa were maintained at −8 °C and 5 °C, respectively. The flow rates of DEZn, TEGa, and O_2 were set to 1, 5, and 250 sccm, respectively. Epitaxial growth was conducted at 700 °C and 740 Pa for 90 minutes. The samples were then annealed in O_2 and Ar atmospheres at 600, 700, 800, and 850 °C for 60 minutes, with a constant gas flow rate of 20 sccm. The crystal structure and phase composition of the thin films were characterized using X-ray diffraction (XRD) (Bruker D8, Cu Kα radiation, λ = 0.154 nm). The Zn content in the films was estimated using energy dispersive X-ray spectroscopy (EDS). The optical properties and surface morphology were examined with a UV-3101PC spectrophotometer, an atomic force microscope (AFM) (Bruker Multimode 8), and a scanning electron microscope (SEM) (Hitachi S-4800). Additionally, the elemental composition of the films was analyzed using X-ray photoelectron spectroscopy (XPS) (Thermo Scientific Escalab 250Xi), with charge calibration performed relative to the C 1s binding energy of 284.8 eV.

Au interdigital electrodes were fabricated on the thin film using photolithography to design the MSM structure. The current–voltage (*I–V*) and photocurrent (*I–t*) characteristics were measured using an Agilent B1500A semiconductor analyzer. The spectral response was evaluated with a 200 W UV-enhanced xenon lamp, a lock-in amplifier, and a monochromator for wavelength-dependent measurements. The response time of devices was characterized using a 244 nm wavelength light from an OPO (optical parametric oscillator) laser system. The laser was operated at a repetition rate of 10 Hz, with each pulse duration of 5 ns.

Results and discussion

The XRD patterns of the as-grown and annealed Zn-alloyed Ga_2O_3 thin films are shown in Fig. 1, and Fig. 1a shows a spectrum in the range of 2θ = 10–70°. For the as-grown Zn-alloyed Ga_2O_3 film, the sharp and strong peak at 2θ = 41.68° can be attributed to the (0006) diffraction peak of the *c*-plane sapphire substrate. The diffraction peaks at 2θ = ∼19.0°, ∼38.4°, and ∼59.2° correspond to the (−201), (−402), and (−603) diffraction peaks of the monoclinic structure of β-Ga_2O_3 (JCPDS no. 043-1012), respectively. To further confirm the crystalline phase of the as-grown thin film, we performed Raman spectroscopy analysis of Ga_2O_3, as shown in Fig. S1 (ESI†). Raman spectroscopy was performed on the as-grown film, and after accounting for the influence of the c-Al_2O_3 substrate, characteristic peaks of β-Ga_2O_3 were observed at 203.6, 351.0, and 661.5 cm^{-1}, which are consistent with previously reported values for the β-phase.[30–32] When the annealing temperature is between 600 °C and 700 °C, there is no significant change in the XRD diffraction peak of the obtained film, indicating that the crystal structure of the film has not changed at the annealing temperature of 600–700 °C. However, at annealing temperatures ranging from 800 °C to 850 °C, significant alterations in the diffraction peaks are observed, suggesting a marked transformation in the crystalline structure due to the higher annealing temperatures.

To provide a clearer representation of the changes in the diffraction peaks, the $ZnGa_2O_4$ and β-Ga_2O_3-related peaks in the XRD spectra were enlarged, as shown in Fig. 1b. At an annealing temperature of 800 °C, the diffraction peak near 2θ = ∼19.0° exhibits significant broadening in the full width at half maximum, while the peaks at 2θ = ∼38.4° and ∼59.2° transition from single to double peaks. When the annealing temperature is further increased to 850 °C, the peak near 2θ = ∼19.0° also splits into two distinct peaks. This pattern is consistent regardless of whether the annealing process is conducted in an Ar or O_2 atmosphere. Comparing the twin

Open Access Article. Published on 22 April 2025. Downloaded on 1/10/2026 3:24:16 PM.
This article is licensed under a Creative Commons Attribution-NonCommercial 3.0 Unported Licence.

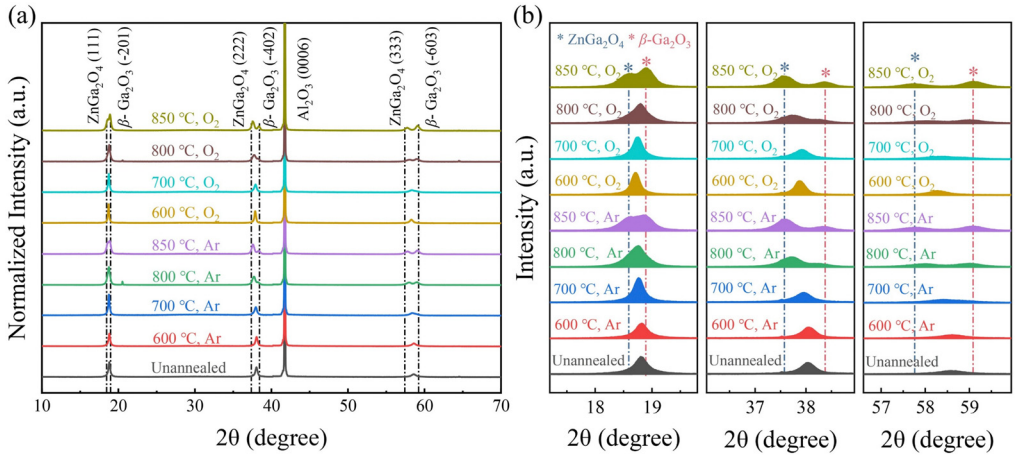

Fig. 1 (a) XRD patterns of the as-grown and annealed films under different conditions. (b) Enlarged sections of the XRD patterns at 2θ = ~19.0°, ~38.4°, and ~59.2°.

peaks appearing in pairs around 2θ = ~19.0°, ~38.4°, and ~59.2° with the JCPDS standard card, it can be found that the peaks with smaller angles are the (111), (222), and (333) peaks of cubic $ZnGa_2O_4$ (JCPDS no. 38-1240), and the peaks with larger angles are the (−201), (−402), and (−603) diffraction peaks of monoclinic β-Ga_2O_3. These findings suggest that annealing at 800 °C or higher facilitates the transformation of single-phase Zn-alloyed Ga_2O_3 thin films into mixed-phase thin films, consisting of both $ZnGa_2O_4$ and β-Ga_2O_3 phases. The diffraction peak of the monoclinic phase in the as-grown thin film shifts to a lower angle compared to the β-Ga_2O_3 peak observed after annealing. This shift in peak positions is likely due to lattice distortion induced by the incorporation of Zn atoms (with ionic radii of 0.74 Å for Zn^{2+} and 0.61 Å for Ga^{3+}).[33] Moreover, the formation of a mixed-phase structure may be attributed to the Zn doping concentration in the as-grown film exceeding the threshold for single-phase Zn-doped Ga_2O_3, as reported in the literature, thus placing the material in a metastable state.[34,35] High-temperature annealing promotes the redistribution of dopant atoms and the relaxation of internal stresses within the film,[36,37] which together contribute to the transition from a single-phase to a mixed-phase structure.

Fig. 2a presents the UV-Vis transmission spectra of the different samples. Across the wavelength range of 300 to 800 nm, all samples exhibited an average transmission exceeding 85%. Moreover, a distinct optical absorption edge was consistently observed within the range of 240–250 nm. The absorption coefficient (α) of the thin film was calculated from the transmission spectrum data. From the obtained α values, $(\alpha h\nu)^2$ and $h\nu$ were subsequently derived. $(\alpha h\nu)^2$ was then plotted *versus* $h\nu$, with $(\alpha h\nu)^2$ on the vertical axis and $h\nu$ on the horizontal axis. The linear region of the resulting curve was fitted to a straight line, and the intercept of this line with the abscissa axis provided the band gap (E_g) of the film.[38] The calculated band gap of the thin film was approximately 5.09–5.11 eV, as indicated in the inset of Fig. 2a. This indicates

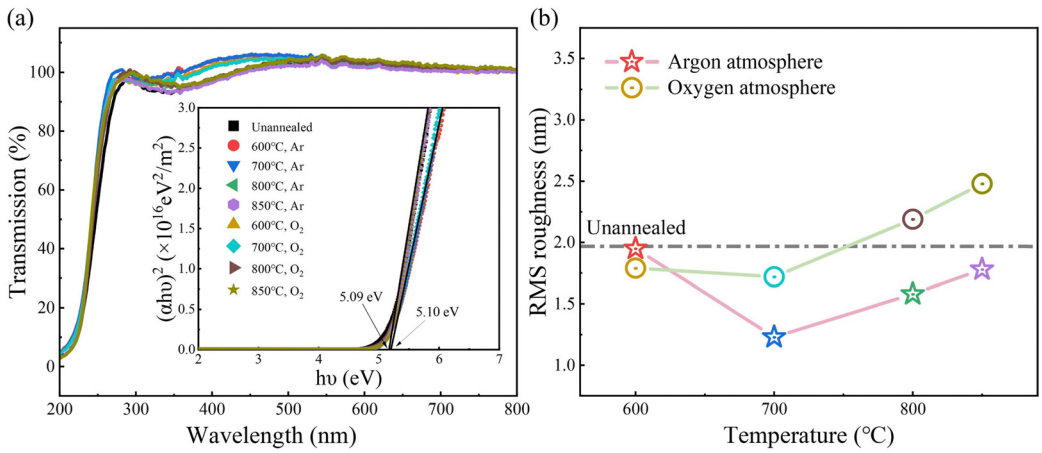

Fig. 2 (a) Transmission spectra of the as-grown and annealed films. The inset shows the corresponding plot of $(\alpha h\nu)^2$ *versus* photon energy $h\nu$ for the different processing conditions. (b) Root-mean-square (RMS) roughness of the films under various treatment conditions, as characterized by AFM.

 This journal is © The Royal Society of Chemistry 2025

Open Access Article. Published on 22 April 2025. Downloaded on 1/10/2026 3:24:16 PM. This article is licensed under a Creative Commons Attribution-NonCommercial 3.0 Unported Licence.

that both high-temperature annealing and material phase separation have minimal influence on the bandgap.

The root-mean-square (RMS) roughness of both the as-grown film and films annealed under various conditions was measured using AFM, with the results shown in Fig. 2b. Detailed 3D surface morphology is provided in Fig. S2 and S3 in the ESI.† For annealing temperatures between 600 °C and 700 °C, the RMS roughness values of the films in both atmospheres exhibited a decreasing trend as the annealing temperature increased. These findings suggest that annealing effectively improves the crystalline quality of the films before phase separation occurs. However, at higher annealing temperatures (800–850 °C), the values gradually increase, which may be attributed to the formation of new grain boundaries caused by pronounced phase separation. Despite these variations in roughness, the changes remained within a narrow range of 1.25 nm to 2.5 nm, and the surfaces of the films remained relatively smooth and uniform.

Fig. 3 illustrates the surface SEM images of Zn-alloyed Ga_2O_3 thin films annealed under different atmospheres and temperatures, with cross-sectional SEM images provided as insets. For comparison, the SEM images of the as-grown films are presented in Fig. S4a and b in the ESI.† As the annealing temperature increases, the surfaces of the films under both atmospheres remain dense, without the formation of large grains. Cross-sectional SEM images reveal a sharp interface between the substrate and the epitaxial films, with the film thickness consistently maintained at approximately 110 nm. Notably, even in the presence of phase separation, no significant changes in surface morphology or the film thickness are observed. EDS analysis (see Fig. S5 and S6 in the ESI†) further confirms that the atomic ratio of Zn to Ga remains nearly constant before and after annealing, with the Zn content stabilized around 15.02%. These findings suggest that, although phase separation occurs during high-temperature annealing at 800–850 °C, no detectable loss of Zn or Ga elements from the films is observed.

Oxygen vacancies are a key factor affecting the performance of oxide semiconductor ultraviolet detectors.[39–41] To better understand their distribution within the thin films, we performed a detailed investigation using XPS. Fig. 4a presents the high-resolution O 1s core-level spectrum of the as-grown Zn-alloyed Ga_2O_3 thin film. The peak at approximately 530.68 eV (O_A) is attributed to lattice oxygen, while the peak at around 531.52 eV (O_B) is associated with oxygen vacancies.[42,43] The oxygen vacancy concentration in the as-deposited film was determined to be 24.2% based on the peak area ratio ($O_B/(O_A + O_B)$). Fig. 4b presents the high-resolution O 1s core-level spectra of films annealed at various temperatures under an Ar atmosphere. The oxygen vacancy concentrations showed a slight increase with annealing temperature, reaching 25.4%, 27.5%, 27.5%, and 28.1% at 600 °C, 700 °C, 800 °C, and 850 °C, respectively. In contrast, Fig. 4c shows the high-resolution O 1s core-level spectra of films annealed under an O_2 atmosphere. For these films, the oxygen vacancy concentrations exhibited a decrease as the annealing temperature increased, from 23.1% at 600 °C to 21.9%, 19.4%, and 16.7% at 700 °C, 800 °C, and 850 °C, respectively. Fig. 4d illustrates the evolution of the oxygen vacancy concentration under varying annealing conditions. With increasing annealing temperature, an Ar atmosphere promotes oxygen vacancy formation, while an O_2 atmosphere inhibits their formation. This divergence can be attributed to distinct annealing mechanisms: in oxygen-deficient environments, oxygen escapes from the film, creating vacancies, whereas in oxygen-rich environments, atmospheric oxygen interacts with the lattice and fills surface oxygen vacancies.[41] These results demonstrate that while annealing in both Ar and O_2 atmospheres induces similar phase separation in the film, their effects on the oxygen vacancy concentration are entirely opposite. The fine Zn 2p spectrum exhibits a binding energy difference of approximately 23 eV between Zn $2p_{1/2}$ and Zn $2p_{3/2}$, while the fine Ga 2p spectrum shows a binding energy difference of approximately 26.9 eV between Ga $2p_{1/2}$ and Ga $2p_{3/2}$ (See Fig. S7, ESI†), both of which are

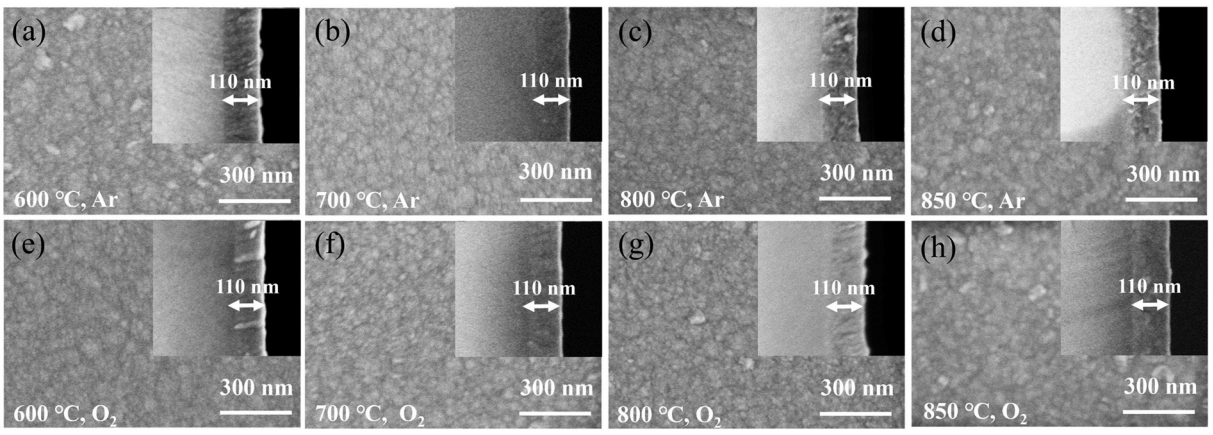

Fig. 3 Surface SEM images of the films annealed under different conditions, with the corresponding cross-sectional SEM images shown in the insets. (a)–(d) Films annealed at various temperatures in an argon atmosphere. (e)–(h) Films annealed at different temperatures in an oxygen atmosphere.

Open Access Article. Published on 22 April 2025. Downloaded on 1/10/2026 3:24:16 PM.
This article is licensed under a Creative Commons Attribution-NonCommercial 3.0 Unported Licence.

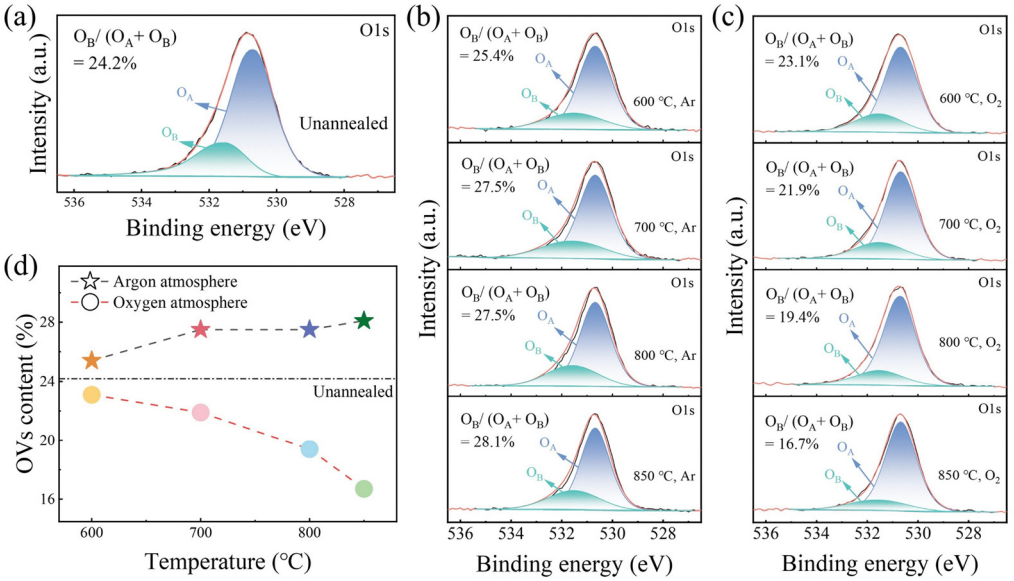

Fig. 4 O 1s core-level XPS spectra of films treated under different conditions. (a) As-grown films. (b) Films annealed in an Ar atmosphere. (c) Films annealed in an O_2 atmosphere. The peak at O_B is attributed to oxygen vacancy defects, while the peak at O_A corresponds to lattice oxygen in the film. The ratio of peak areas ($O_B/(O_A + O_B)$) serves as an indicator of the oxygen vacancy concentration within the film. (d) Changes in the oxygen vacancy concentration under various annealing atmospheres and temperature conditions.

consistent with reference values.[44] The binding energy difference between the Zn $2p_{3/2}$ and Ga $2p_{3/2}$ peaks serves as a parameter for differentiating $ZnGa_2O_4$ from a mixture of ZnO and Ga_2O_3.[45,46] The calculated binding energy difference of 95.9 eV closely aligns with the expected value for $ZnGa_2O_4$ formation.

To investigate the photoelectric properties of two groups of thin films, Au interdigitated electrodes were fabricated using photolithography and lift-off techniques. The electrodes were designed with a length of 500 μm, a width of 10 μm, an interfinger spacing of 10 μm, and 25 pairs of fingers. These electrodes were incorporated into an MSM-structured ultraviolet photodetector. The schematic of the device structure is shown in Fig. 5a, with the effective illuminated area measured as 0.5 mm^2. Fig. 5b and c display the *I–V* characteristics of the annealed device in a dark environment. Devices fabricated

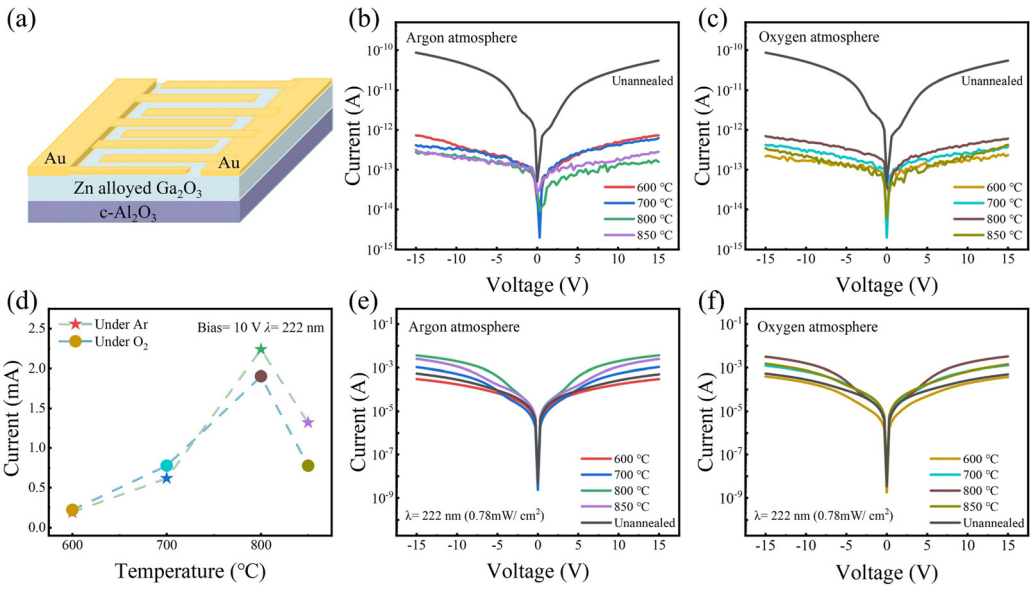

Fig. 5 (a) Schematic diagram of the MSM detector structure. (b) *I–V* characteristics of the detector based on the films annealed in an Ar atmosphere (dark environment). (c) *I–V* characteristics of the detector based on the films annealed in an O_2 atmosphere (dark environment). (d) Photocurrent response trends for different devices. (e) *I–V* characteristics of the detector based on the films annealed in an Ar atmosphere (illuminated with UV light, λ = 222 nm). (f) *I–V* characteristics of the detector based on the films annealed in an O_2 atmosphere (illuminated with UV light, λ = 222 nm).

 This journal is © The Royal Society of Chemistry 2025

Open Access Article. Published on 22 April 2025. Downloaded on 1/10/2026 3:24:16 PM.
This article is licensed under a Creative Commons Attribution-NonCommercial 3.0 Unported Licence.

using as-grown thin films exhibited a dark current of 32 pA under an applied bias of 10 V. After annealing, the dark current was drastically reduced to below 1 pA, indicating a significant enhancement in device performance. The *I–V* characteristics of the annealed devices under ultraviolet illumination (wavelength: 222 nm, power density: 0.78 mW cm^{-2}) are shown in Fig. 5e and f. The data indicate that the photocurrent increases steadily with annealing temperatures ranging from 700 °C to 800 °C, irrespective of whether the annealing atmosphere is oxygen or argon. At 850 °C, the photocurrent decreases slightly, however, it remains higher than the value observed at 700 °C. To provide a clearer depiction of this trend, Fig. 5d plots the photocurrent at a bias voltage of 10 V as a function of the annealing temperature, offering an intuitive visualization of the relationship between annealing conditions and device performance. Oxygen vacancies are well-established as critical factors influencing device responsivity.[39] However, in this study, analysis of oxygen vacancy concentrations measured by XPS, in conjunction with the performance of devices annealed under different atmospheres, reveals that variations in device performance with annealing temperature are not primarily attributable to changes in oxygen vacancy concentrations. Combined with the previous XRD characterization results, it can be deduced that phase separation occurs in the thin film at 800 °C, coinciding with a significant increase in photoresponsivity. This improvement can be attributed to the formation of mixed-phase heterojunction interfaces, which enhance the generation and transport of photogenerated carriers.[47,48] At 850 °C, pronounced phase separation likely results in the formation of larger energy barriers at the heterojunction interfaces. These barriers impede the efficient transport of photogenerated carriers, thereby leading to a decline in photoresponsivity.[24]

To further investigate the response speed of the devices, the transient photoresponse measurement was carried out using an OPO laser system with a wavelength of 244 nm. The laser pulse width and the repetition rate are 5 ns and 10 Hz, respectively. The test results are shown in Fig. 6. In Fig. 6a, a good reproducibility of photodetectors based on the as-grown film can be clearly observed. To calculate the response time of the device, one cycle is selected, and its magnified image is shown in inset. The 10–90% rise time (defined as the time for the current increasing from 10% to 90% of the peak value) of the device is 0.02 ms. In addition, the 90–10% decay time (defined as the time for the current dropping from 90% to 10% of the peak value) of the device is 2.24 ms. Fig. 6b and c show the transient response curves of devices prepared based on films annealed under different atmospheres and temperatures. It can be seen that the repeatability of the transient response current does not change with annealing conditions. The 10–90% rise time of the devices is very short, around 0.02 ms, while the 90–10% decay time of the devices changes to some extent with the annealing temperature. Fig. 6d shows the trend of the 90–10% decay time with annealing temperature variation. At the same annealing temperature, annealing under oxygen is more conducive to shortening the descent time. When the annealing temperature is between 600 and 700 °C, the decay time is shorter than that of devices based on the as-grown films, and when the annealing temperature reaches 850 °C, the decay time significantly increases. This may be due to the formation of a large number of carrier traps at heterogeneous interfaces within the mixed-phase material, resulting in a significant increase in carrier lifetime.

The responsivity spectra of the device were measured under a bias voltage of 10 V using a monochromator over a wavelength range of 230–500 nm, as shown in Fig. 7a and b. The

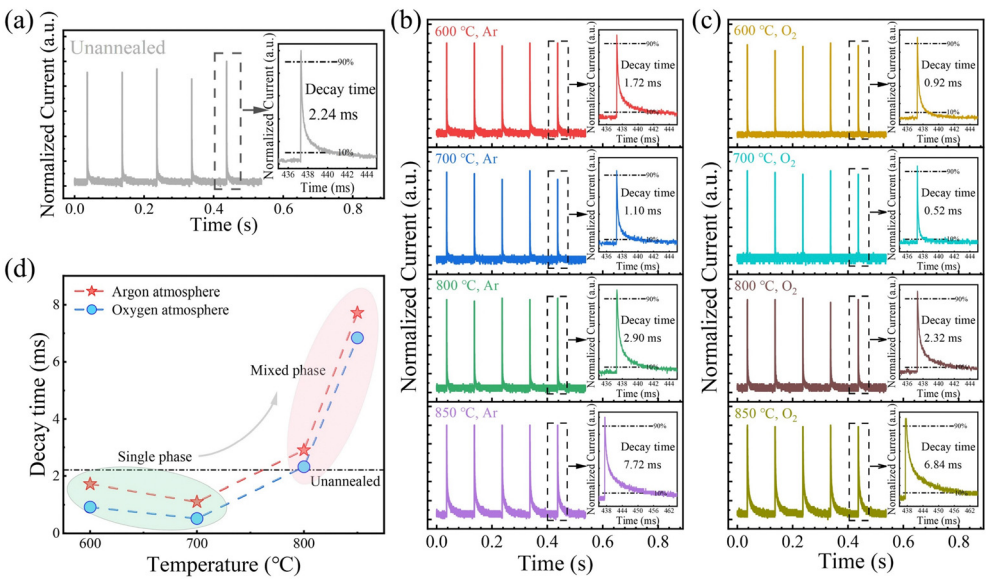

Fig. 6 Transient response curve of photodetectors under 244 nm pulsed laser irradiation. Insets are the enlarged images of a single pulse cycle. (a) Photodetectors based on the as-grown film. (b) Photodetectors based on films annealed in an Ar atmosphere. (c) Photodetectors based on films annealed in an O_2 atmosphere. (d) Trend of the 90–10% decay time with annealing temperature variations.

Open Access Article. Published on 22 April 2025. Downloaded on 1/10/2026 3:24:16 PM. This article is licensed under a Creative Commons Attribution-NonCommercial 3.0 Unported Licence.

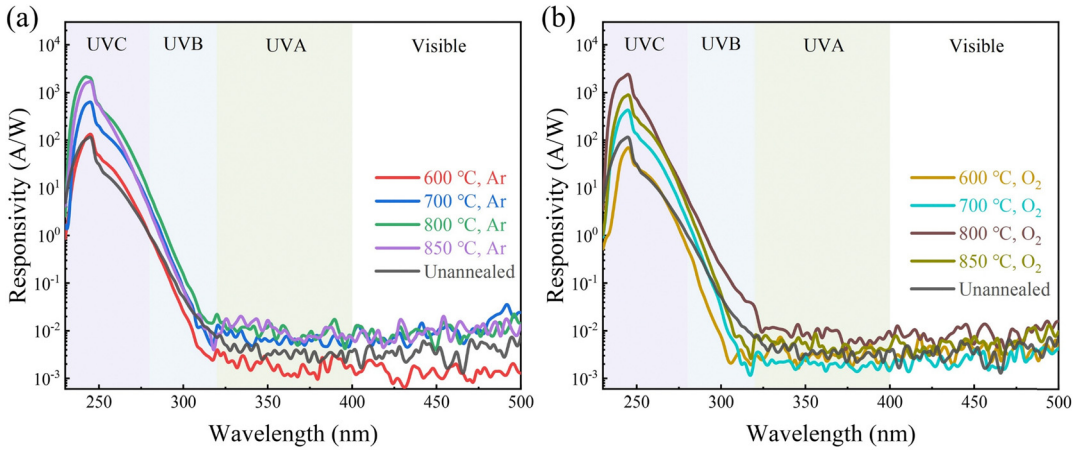

Fig. 7 Responsivity spectra of the devices based on (a) films annealed in an Ar atmosphere and (b) films annealed in an O_2 atmosphere.

responsivity of the detector increases with the annealing temperature and reaches its maximum value when the film transforms into a mixed-phase state and decreases as phase separation becomes more pronounced. When the annealing temperature is 800 °C, the device exhibits optimal photoelectric response performance. The peak responsivity is observed at approximately 244 nm, and the −3 dB cut-off wavelength is around 248 nm. These results indicate that the devices have good solar-blind ultraviolet photoresponse characteristics. When the annealing temperature is 800 °C, the responsivity of devices prepared based on films annealed under Ar and O_2 conditions is 2058.54 A W^{-1} and 2364.01 A W^{-1}, respectively. In addition, the UV-visible rejection ratio, defined as the ratio between the peak responsivity and responsivity at 400 nm, is 3.39×10^5 and 4.75×10^5, respectively.

The specific detectivity (D^*), which serves as a measure of the signal-to-noise ratio, was determined using eqn (1)

$$D^* = \frac{\sqrt{B \cdot S_{\text{eff}}}}{\text{NEP}} \quad (1)$$

where B denotes the measurement bandwidth (12.5 Hz), S_{eff} represents the effective illuminated area of the device (0.5 mm^2), and NEP stands for the noise-equivalent power. To account for the low-frequency noise characteristics of the device, the detector was placed in a dark environment, and a long-term I–t curve was recorded. The dark current curve was analyzed using Fourier transform to determine the frequency–amplitude relationship, facilitating the extraction and evaluation of the corresponding noise spectral density curve. After fitting, the measured low-frequency noise of the device was found to be consistent with $1/f$ noise,[49] as shown in Fig. S8 (ESI†). The total noise current (i_{noise}) was obtained by integrating the noise spectral density curve, and the calculated i_{noise} values for devices annealed in two different atmospheres were found to be $i_{\text{noise-Ar}} = 1.605 \times 10^{-13}$ A and $i_{\text{noise-O}_2} = 1.875 \times 10^{-13}$ A. The relationship between the i_{noise} and NEP is expressed as: NEP = i_{noise}/R, where R represents the responsivity of the device.[50,51] Accordingly, eqn (1) can be rewritten as eqn (2)

$$D^* = \frac{R\sqrt{B \cdot S_{\text{eff}}}}{i_{\text{noise}}} \quad (2)$$

The performance metrics of devices subjected to different annealing conditions are summarized in Table S1 (ESI†). A comparative analysis reveals that devices with mixed-phase films annealed at 800 °C exhibit superior overall performance. While an increase in the degree of phase mixing leads to a slight decline in device performance, it remains higher than that of devices with non-phase-separated thin films. These findings suggest that Zn alloying, followed by annealing to induce mixed-phase formation, is an effective strategy for optimizing the film structure and enhancing the optoelectronic performance of detectors. The performance metrics of devices annealed at 800 °C with mixed-phase structures, as summarized in Table 1, were compared to those of previously reported single-phase and mixed-phase devices. Notably, our devices exhibit significantly enhanced ultraviolet photodetection performance. This improvement is attributed to the formation of mixed-phase heterojunction structures induced by the annealing of β-Ga_2O_3 doped with high Zn content, which significantly enhances the performance of solar-blind ultraviolet photodetectors.

The substantial enhancement in device performance observed at an annealing temperature of 800 °C may be attributed to the formation of heterojunction interfaces between the mixed-phases within the thin films. The operation mechanism of the solar-blind photodetector based on Ga_2O_3/$ZnGa_2O_4$ mixed-phase films is proposed and schematically presented in Fig. 8. Fig. 8a presents a schematic representation of the crystal phase structure within the mixed-phase film. Under thermal equilibrium conditions (Fig. 8b), the high density of interface states results in recombination centers being primarily localized at the heterojunction interface between Ga_2O_3 and $ZnGa_2O_4$, where electrons and holes overcome the potential barrier and recombine. When a bias voltage

 This journal is © The Royal Society of Chemistry 2025

Open Access Article. Published on 22 April 2025. Downloaded on 1/10/2026 3:24:16 PM.
This article is licensed under a Creative Commons Attribution-NonCommercial 3.0 Unported Licence.

Table 1 Performance comparison of various Ga_2O_3-based ultraviolet detectors

Materials	Method	Bias (V)	Dark current (pA)	Responsivity (A W^{-1})	Decay time (ms)	Detectivity (cm $Hz^{1/2}$ W^{-1})	Ref.
β-Ga_2O_3	CVD	5	~100	9.5×10^3	10	1.5×10^{15}	52
β-Ga_2O_3	M.E.[a]	5	12.09	44.09	27.74	5.84×10^{12}	53
β-Ga_2O_3	MBE	10	4.2	83.3	690	1.35×10^{15}	54
β-Ga_2O_3	MOCVD	10	29	38.82	500	9×10^{15}	55
β-Ga_2O_3	MOCVD	20	0.635	72.35	8	—	56
β-Ga_2O_3	MOCVD	0	—	0.25	0.031	—	57
α-Ga_2O_3	MBE	−5	<1	0.5	0.238	9.66×10^{12}	58
β-Ga_2O_3:Zn	MOCVD	20	~10	210	1400	—	59
β-Ga_2O_3:Zn	MOCVD	10	37	2.8×10^3	240	5.9×10^{16}	35
$ZnGa_2O_4$	PLD	5	8.56	1.97	400	—	60
$ZnGa_2O_4$	MOCVD	5	0.916	639	400	—	61
m-InGaO	CVD	10	0.03	0.97	260	4.62×10^{14}	29
m-Ga_2O_3/SnO_2	CVD	40	11	0.32	1708	2×10^{13}	28
m-MgZnO	MBE	10	4	32	37	—	48
m-Ga_2O_3/$ZnGa_2O_4$	MOCVD	10	0.137	2058.54	2.90	3.21×10^{15}	This work
m-Ga_2O_3/$ZnGa_2O_4$	MOCVD	10	0.453	2364.01	2.32	3.15×10^{15}	This work

Note: [a] M. E. means mechanical exfoliation.

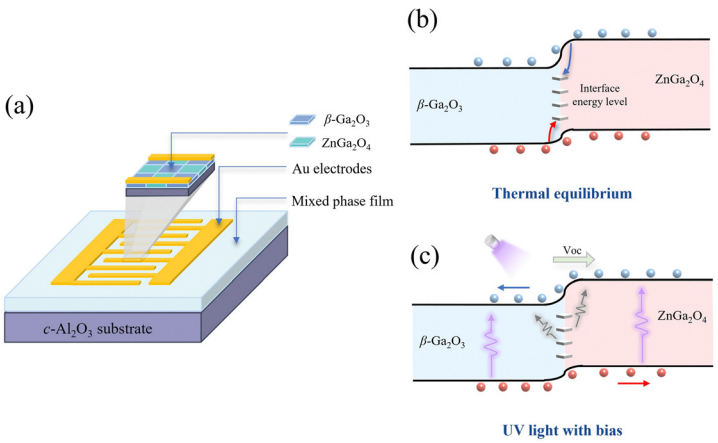

Fig. 8 Energy band diagrams and the carrier transport process in the mixed-phase detector. (a) Schematic representation of the crystal phase structure within the mixed-phase film. (b) Under thermal equilibrium conditions. (c) Under applied bias with ultraviolet light illumination. The schematics depict the flow of charge carriers, with blue spheres representing electrons and red spheres representing holes.

and ultraviolet illumination are applied, the energy band structure transitions to the configuration shown in Fig. 8c, and the interface states capture holes from the newly generated photogenerated carriers. The internal photoconductive gain of the detector can be described by eqn (3)

$$G = \tau \cdot \frac{1}{t_{rn}} \quad (3)$$

where τ represents the lifetime of photo-generated holes, and t_m denote the transit times of electrons. The presence of interface states extends the carrier lifetime, thereby significantly enhancing the photocurrent. Furthermore, the heterojunction interface broadens the built-in electric field and introduces a potential barrier, which restricts the drift motion of majority carriers and effectively suppresses the dark current, ensuring that it remains at a low level.[48] By optimizing the degree of phase mixing within the thin film, the response time can be controlled within an acceptable range, achieving a balance between the rapid response and high responsivity. These optimizations contribute to the enhanced overall performance of solar-blind ultraviolet detectors.

Conclusions

High-Zn-content doped β-Ga_2O_3 films were epitaxially grown on c-Al_2O_3 substrates using MOCVD. Annealing at temperatures above 800 °C induced a Ga_2O_3/$ZnGa_2O_4$ mixed-phase structure in the films. A photodetector with a simple MSM structure, fabricated from films annealed at 800 °C in an Ar atmosphere, demonstrated superior performance. Under a 10 V bias, the device exhibited a low dark current (0.137 pA), high photoresponse (2058.54 A W^{-1}), detectivity (3.21×10^{15} cm $Hz^{1/2}$ W^{-1}), and rapid response speed (decay time 2.90 ms). Through the analysis of oxygen vacancy concentrations under O_2 and Ar atmospheres and their correlation with device performance, we have ruled out oxygen vacancies as the primary factor influencing device behavior. Instead, the enhanced performance of the ultraviolet detector is attributed to the formation of a

Open Access Article. Published on 22 April 2025. Downloaded on 1/10/2026 3:24:16 PM.
This article is licensed under a Creative Commons Attribution-NonCommercial 3.0 Unported Licence.

mixed-phase heterojunction interface. These findings contribute to a deeper understanding of mixed-phase material systems and provide important guidance for the development and optimization of high-performance ultraviolet detectors.

Author contributions

The manuscript was written through contributions from all authors. All authors have given approval to the final version of the manuscript.

Data availability

The authors confirm that the data supporting the findings of this study are available within the article.

Conflicts of interest

The authors declare no competing financial interest.

Acknowledgements

This work is supported by the National Natural Science Foundation of China (12204474, 12304111, 12304112, 62074148 and 11727902), the Jilin Province Young and Middle-aged Science and Technology Innovation Leaders and Team Project (20220508153RC), the Jilin Province Science Fund (20220101053JC), the Youth Innovation Promotion Association, CAS (2020225), and the Provincial Science and Technology Major Project of Jiangsu (BG2024030).

References

1 Z. Li, T. Yan and X. Fang, *Nat. Rev. Mater.*, 2023, **8**, 587–603.
2 C. Xie, X. T. Lu, X. W. Tong, Z. X. Zhang, F. X. Liang, L. Liang, L. B. Luo and Y. C. Wu, *Adv. Funct. Mater.*, 2019, **29**, 1806006.
3 X. Chen, F. Ren, S. Gu and J. Ye, *Photon. Res.*, 2019, **7**, 381–415.
4 X. He, R. Sun, X. Xu, H. Geng, S. Qi, K. H. Zhang and H. Long, *ACS Appl. Mater. Interfaces*, 2024, **16**, 64146–64155.
5 U. Varshney, N. Aggarwal and G. Gupta, *J. Mater. Chem. C*, 2022, **10**, 1573–1593.
6 J. Ding, P. Zhao, H. Chen and H. Fu, *Appl. Phys. A*, 2024, **130**, 350.
7 J. Shi, J. Zhang, L. Yang, M. Qu, D. C. Qi and K. H. L. Zhang, *Adv. Mater.*, 2021, **33**, 2006230.
8 Z. Wang, R. Yu, X. Wang, W. Wu and Z. L. Wang, *Adv. Mater.*, 2016, **28**, 6880–6886.
9 P. Vashishtha, I. H. Abidi, S. P. Giridhar, A. K. Verma, P. Prajapat, A. Bhoriya, B. J. Murdoch, J. O. Tollerud, C. Xu, J. A. Davis, G. Gupta and S. Walia, *ACS Appl. Mater. Interfaces*, 2024, **16**, 31294–31303.
10 L. Cheng, Y. Wu, W. Cai and W. Zheng, *Mater. Today Phys.*, 2023, **36**, 101164.
11 M. M. Fan, K. W. Liu, Z. Z. Zhang, B. H. Li, X. Chen, D. X. Zhao, C. X. Shan and D. Z. Shen, *Appl. Phys. Lett.*, 2014, **105**, 011117.
12 S. Han, H. Xia, Y. M. Lu, W. J. Liu, W. Y. Xu, M. Fang, P. J. Cao and D. L. Zhu, *Nanotechnology*, 2021, **32**, 235202.
13 S. Han, D. Yue, P. Cao, W. Liu, Y. Zeng, M. Fang and D. Zhu, *Opt. Mater.*, 2024, **147**, 114612.
14 J. Zhang, J. Shi, D.-C. Qi, L. Chen and K. H. L. Zhang, *APL Mater.*, 2020, **8**, 020906.
15 C. Xie, X. Lu, Y. Liang, H. Chen, L. Wang, C. Wu, D. Wu, W. Yang and L. Luo, *J. Mater. Sci. Technol.*, 2021, **72**, 189–196.
16 S. Kim, Y. Yoon, D. Seo, J.-H. Park, D.-W. Jeon, W. S. Hwang and M. Shin, *APL Mater.*, 2023, **11**, 061107.
17 H. Huang, H. Yin, K. Han, Y. Wang, Z. Wang, X. Feng, Y. Zou, X. Zhou, G. Xu, X. Hou, X. Zhao and S. Long, *Adv. Opt. Mater.*, 2024, **12**, 2400788.
18 J. Zhang, X. Kuang, R. Tu and S. Zhang, *Adv. Colloid Interface Sci.*, 2024, **328**, 103175.
19 Z. Wang, G. Zhang, X. Zhang, C. Wu, Z. Xia, H. Hu, F. Wu, D. Guo and S. Wang, *Adv. Opt. Mater.*, 2024, **12**, 2401256.
20 C. Wu, F. Wu, H. Hu, S. Wang, A. Liu and D. Guo, *Mater. Today Phys.*, 2022, **28**, 100883.
21 C. Wu, T. Zhao, H. He, H. Hu, Z. Liu, S. Wang, F. Zhang, Q. Wang, A. Liu, F. Wu and D. Guo, *Adv. Opt. Mater.*, 2024, **12**, 2302294.
22 Y. M. Lu, C. Li, X. H. Chen, S. Han, P. J. Cao, F. Jia, Y. X. Zeng, X. K. Liu, W. Y. Xu, W. J. Liu and D. L. Zhu, *Chin. Phys. B*, 2019, **28**, 018504.
23 S. Ganguly, K. Nama Manjunatha and S. Paul, *Phys. Status Solidi RRL*, 2023, **18**, 2300296.
24 H. Liu, H. Li, S. Zhou, H. Zhang, S. Fan, Y. Cui, C. Kong, L. Ye, Y. Xiong and W. Li, *Crystals*, 2021, **11**, 1111.
25 A. A. Mohammed and W. Foong Lim, *Mater. Sci. Eng. B*, 2024, **308**, 117613.
26 F. Zhang, J. Sun, H. Li, J. Zhou, T. Sun, T. Fu, G. Xiao, Y. Chen, Y. Deng and J. Zhai, *J. Electron. Mater.*, 2019, **48**, 8061–8066.
27 Y.-C. Chen, G. Zeng, S.-T. Ding, C.-Y. Shi, X.-F. Zhao, D. W. Zhang and H.-L. Lu, *ACS Mater. Lett.*, 2023, **5**, 2852–2861.
28 M.-M. Fan, L. Cao, K.-L. Xu and X.-Y. Li, *J. Alloys Compd.*, 2021, **853**, 157080.
29 K. Qi, S. Fu, Y. Wang, Y. Han, R. Fu, C. Gao, J. Ma, H. Xu, B. Li, A. Shen and Y. Liu, *J. Alloys Compd.*, 2023, **965**, 171473.
30 B. M. Janzen, P. Mazzolini, R. Gillen, A. Falkenstein, M. Martin, H. Tornatzky, J. Maultzsch, O. Bierwagen and M. R. Wagner, *J. Mater. Chem. C*, 2021, **9**(7), 2311–2320.
31 H. Cui, H. F. Mohamed, C. Xia, Q. Sai, W. Zhou, H. Qi, J. Zhao, J. Si and X. Ji, *J. Alloys Compd.*, 2019, **788**, 925–928.
32 C. Kranert, C. Sturm, R. Schmidt-Grund and M. Grundmann, *Sci. Rep.*, 2016, **6**, 35964.
33 S. Gao, W. Li, J. Dai, Q. Wang and Z. Suo, *Mater. Res. Express*, 2021, **8**, 025904.
34 E. Chikoidze, C. Sartel, I. Madaci, H. Mohamed, C. Vilar, B. Ballesteros, F. Belarre, E. del Corro, P. Vales-Castro,

 This journal is © The Royal Society of Chemistry 2025

Open Access Article. Published on 22 April 2025. Downloaded on 1/10/2026 3:24:16 PM.
This article is licensed under a Creative Commons Attribution-NonCommercial 3.0 Unported Licence.

G. Sauthier, L. Li, M. Jennings, V. Sallet, Y. Dumont and A. Pérez-Tomás, *Cryst. Growth Des.*, 2020, **20**, 2535–2546.
35 X. Sun, K. Liu, X. Chen, Q. Hou, Z. Cheng, J. Yang, Q. Ai, Y. Zhu, B. Li, L. Liu and D. Shen, *J. Mater. Chem. C*, 2023, **11**, 3227–3234.
36 S. S. Shankar, U. Manzoor, D. K. Kim, M. Islam and A. S. Bhatti, *PLoS One*, 2014, **9**, e86418.
37 H. Lee, S. Kim, H. Ahn, K. Kim and M. Yang, *Cryst. Res. Technol.*, 2020, **56**, 2000149.
38 S. S. Kumar, E. J. Rubio, M. Noor-A-Alam, G. Martinez, S. Manandhar, V. Shutthanandan, S. Thevuthasan and C. V. Ramana, *J. Phys. Chem. C*, 2013, **117**, 4194–4200.
39 L. Dong, R. Jia, B. Xin, B. Peng and Y. Zhang, *Sci. Rep.*, 2017, **7**, 40160.
40 J. Wang, X. Ji, Z. Yan, S. Qi, X. Liu, A. Zhong and P. Li, *J. Alloys Compd.*, 2024, **970**, 172448.
41 M. Narayanan, A. P. Shah, S. Ghosh, A. Thamizhavel and A. Bhattacharya, *Appl. Phys. Lett.*, 2023, **123**, 172106.
42 H. Huang, L. Wang, H. Zhou, H. Xing, L. Wang, W. Zhang, K. Tang, J. Huang and L. Wang, *ACS Appl. Mater. Interfaces*, 2024, **16**, 63808–63817.
43 L. Gu, H.-P. Ma, Y. Li, A.-F. Wang, W.-J. Chen, Z.-R. Tang, Y. Shen, F. Y. Sun, J.-T. Zhu and Q.-C. Zhang, *Appl. Surf. Sci.*, 2023, **641**, 158502.
44 X. Duan, F. Yu and Y. Wu, *Appl. Surf. Sci.*, 2012, **261**, 830–834.
45 A. R. Phani, S. Santucci, S. DiNardo, L. Lozzi, M. Passacantando, P. Picozzi and C. Cantalni, *J. Mater. Sci.*, 1998, **33**, 3969–3973.
46 Y. Xin, Z. Gao, X. Shang, J. Wu, D. Yu, J. Xiu and Z. Li, *J. Alloys Compd.*, 2023, **933**, 167760.
47 D. Li, R. Deng, Y. Li and D. Jiang, *ACS Appl. Mater. Interfaces*, 2024, **16**, 45156–45165.
48 M.-M. Fan, K.-W. Liu, X. Chen, X. Wang, Z.-Z. Zhang, B.-H. Li and D.-Z. Shen, *ACS Appl. Mater. Interfaces*, 2015, **7**, 20600–20606.
49 Q. Chen, J. W. Yang, A. Osinsky, S. Gangopadhyay, B. Lim, M. Z. Anwar, M. A. Khan, D. Kuksenkov and H. Temkin, *Appl. Phys. Lett.*, 1997, **70**, 2277–2279.
50 H.-Y. Lee, J.-T. Liu and C.-T. Lee, *IEEE Photonics Technol. Lett.*, 2018, **30**, 549–552.
51 Y. Fang, A. Armin, P. Meredith and J. Huang, *Nat. Photonics*, 2018, **13**, 1–4.
52 Z. X. Jiang, Z. Y. Wu, C. C. Ma, J. N. Deng, H. Zhang, Y. Xu, J. D. Ye, Z. L. Fang, G. Q. Zhang, J. Y. Kang and T. Y. Zhang, *Mater. Today Phys.*, 2020, **14**, 100226.
53 S. Qi, J. Liu, J. Yue, X. Ji, J. Shen, Y. Yang, J. Wang, S. Li, Z. Wu and W. Tang, *J. Mater. Chem. C*, 2023, **11**, 8454–8461.
54 J. Tian, X. Song, S. Yang, B. Chen, S. Lei, X. Zhang and L.-X. Qian, *IEEE Trans. Electron Devices*, 2024, **71**, 3746–3752.
55 C. Zhang, K. Liu, Q. Ai, X. Huang, X. Chen, Y. Zhu, J. Yang, Z. Cheng, B. Li, L. Liu and D. Shen, *J. Phys. Chem. C*, 2022, **126**, 21839–21846.
56 Y. Yuan, Z. Li, X. Hou, X. Zhao, M. Ding, S. Yu, Z. Wang, J. Liu, G. Xu, Z. Jia, X. Tao, W. Mu and S. Long, *J. Alloys Compd.*, 2023, **969**, 171596.
57 Z. Cai, X. He, K. Wang, X. Hou, Y. Mei, L. Ying, B. Zhang and H. Long, *Small Methods*, 2023, **8**, 2301148.
58 X. Chen, Y. Xu, D. Zhou, S. Yang, F.-F. Ren, H. Lu, K. Tang, S. Gu, R. Zhang, Y. Zheng and J. Ye, *ACS Appl. Mater. Interfaces*, 2017, **9**, 36997–37005.
59 F. Alema, B. Hertog, O. Ledyaev, D. Volovik, G. Thoma, R. Miller, A. Osinsky, P. Mukhopadhyay, S. Bakhshi, H. Ali and W. V. Schoenfeld, *Phys. Status Solidi A*, 2017, **214**, 1600688.
60 C.-C. Yen, A. K. Singh, H. Chang, K.-P. Chang, P.-W. Chen, P.-L. Liu and D.-S. Wuu, *Appl. Surf. Sci.*, 2022, **597**, 153700.
61 A. Sood, F.-G. Tarntair, Y.-X. Wang, T.-C. Chang, Y.-H. Chen, P.-L. Liu and R.-H. Horng, *Results Phys.*, 2021, **29**, 104764.